ADVANCED MATERIALS
www.advmat.de

Flexible and Dynamic Interfacial Desolvation in High-Entropy Electrolyte for Dendrite-Free Aqueous Zinc-Ion Batteries

Rui Pan, Yucheng Xie, Bowen Jiang, Tong Liu, YingYu Han, Zhipeng Shao, Andreu Cabot, Shulin Jiao, Litao Sun, Kuibo Yin,* and Qichong Zhang**

Aqueous zinc-ion batteries are promising candidates beyond lithium-ion technologies, but the intrinsic hydrogen-down orientation of interfacial water under negative bias, together with ion depletion at the electrode surface, promotes inhomogeneous Zn plating and substantial hydrogen evolution. Here, a high-entropy flexible electrolyte (HEFE) is demonstrated that leverages the fast water-exchange kinetics of Li^+, K^+, and Cs^+. By deliberately inducing cation-hydration disequilibrium, the HEFE forms flexible $Zn(H_2O)_m^{2+}$ ($m \leq 6$) solvation structures embedded in a disordered water network, enhancing ionic conductivity and alleviating ion-transport limitations. Under cathodic bias, a progressive desolvation from $Zn(H_2O)_6^{2+}$ to $Zn(H_2O)_x^{2+}$ ($x \leq 5$) proceeds while retaining aqueous disorder, thereby suppressing hydrogen evolution and enabling 3500 h of deep cycling at 1 mA cm^{-2}/3 mAh cm^{-2}. For iodine cathodes, the HEFE induces a pathway shift from the conventional $I^- \rightarrow I_2$ route to a solid–solid ($CsI \rightarrow I_2$) conversion, fundamentally inhibiting iodide shuttling and extending full-cell life to 3600 cycles at 1 A g^{-1}. Beyond Zn, the solvation-heterogeneity strategy opens avenues for reversible multivalent electrochemistry and advancing next-generation energy-storage systems.

1. Introduction

Amid the global drive to decarbonize industries and mitigate climate change, lithium-ion batteries have come to dominate energy-storage markets.[1–5] Yet intrinsic limitations, most notably electrolyte flammability and constrained lithium resources, challenge their sustainable scalability and motivate the search for alternatives.[6,7] Aqueous zinc-ion batteries (AZIBs) have emerged as strong candidates for stationary storage, leveraging zinc abundance, non-flammability, high theoretical capacity (820 mAh g^{-1}), and a favorable redox potential.[8–10] In aqueous media, Zn^{2+} ions form $[Zn(H_2O)_6]^{2+}$ solvation complexes where strong electrostatic interactions polarize the coordinated water molecules and shift hydrolysis equilibria, imparting moderate acidity. Although proton reduction is thermodynamically favored, Zn anodes can remain electrochemically reversible because the hydrogen evolution reaction (HER) exhibits a high overpotential (≈0.8 V) on Zn surfaces.[11] Unlike conventional redox systems, AZIBs operate under intense interfacial electric fields (>10^5 V m^{-1}) that profoundly influence interfacial-water orientation, double-layer structure, and desolvation kinetics, with direct consequences for Zn nucleation/growth and HER behavior.[12] Despite their pivotal role in dictating AZIB performance, the coupled electrochemical–electrostatic phenomena within the nanoconfined Zn/electrolyte interface remain insufficiently understood, underscoring the need for systematic studies of solvation structure, interfacial water orientation, and field-driven transport to suppress HER and achieve uniform Zn deposition.

R. Pan, B. Jiang, L. Sun, K. Yin
SEU-FEI Nano-Pico Center
Key Laboratory of MEMS of Ministry of Education
Southeast University
Nanjing 210096, China
E-mail: yinkuibo@seu.edu.cn

Y. Xie, T. Liu, Y. Han, Z. Shao, Q. Zhang
Key Laboratory of Multifunctional Nanomaterials and Smart Systems
Suzhou Institute of Nano-Tech and Nano-Bionics
Chinese Academy of Sciences
Suzhou 215123, China
E-mail: qczhang2016@sinano.ac.cn

S. Jiao
Collaborative Innovation Center of Advanced Microstructures Laboratory of Solid State Microstructures & School of Physics
Nanjing University
Nanjing 210093, China

A. Cabot
Catalonia Energy Research Institute-IREC
Sant Adrià de Besòs, Barcelona, Catalonia 08930, Spain
E-mail: acabot@irec.cat

A. Cabot
ICREA
Pg. Lluis Companys 23, Barcelona, Catalonia 08010, Spain

The ORCID identification number(s) for the author(s) of this article can be found under https://doi.org/10.1002/adma.202512633

DOI: 10.1002/adma.202512633

Electrolyte engineering, via compositional modification and concentration tuning, has emerged as a key strategy for improving AZIB performance.[13–18] Among these approaches, the incorporation of additives to modulate the solvation enthalpy of Zn^{2+} ions, thereby influencing water behavior at the electrode-electrolyte interface, has proven particularly effective.[19–23] In particular, highly soluble organic additives, such as ethylene glycol and butanone, often drive ligand exchange, yielding water-deficient $[Zn(organic)_x(H_2O)_y]^{2+}$ complexes with weakened ion–solvent interactions and lower ion–water binding energies.[24,25] Although this targets the inherent electrochemical reactivity of water, organic additives can introduce environmental and toxicological risks and degrade cathode performance.[22,26] To mitigate these drawbacks, concentrated electrolytes, such as water-in-salt electrolytes (WISE), have gained attention for suppressing water decomposition by lowering water activity and limiting its participation in side reactions.[27–29] Wang et al. pioneered the deployment of WISE systems, demonstrating that insufficient hydration shells impede parasitic reactions and broaden the operational voltage window.[30,31] Thermodynamically, solubility and solvation are governed by the free energy change:

$$\Delta G_{sol} = \Delta H_{sol} - T\Delta S_{sol} \quad (1)$$

While increasing concentration can lower ΔH_{sol} through enthalpically favorable ion pairing and "free" additional water to sustain high salt loading, it can also promote ordered ionic clusters, increase viscosity, slow ion migration, delay interfacial ion supply, and reinforce hydrogen-down water orientation under negative bias. These effects create inherent trade-offs in concentrated electrolytes: gains in water-reactivity suppression and stability can be offset by penalties in transport kinetics and interfacial dynamics. Consequently, effective electrolyte design requires balancing salt identity, additive chemistry, and concentration to tune solvation structure, water activity, and bulk/interfacial transport without compromising environmental compatibility or cathode performance.

A paradigm shift from enthalpy-driven to entropy-driven electrolyte design may offer a better balance.[32] Increasing configurational entropy by diversifying compositions is an effective way to navigate the trade-offs inherent to concentrated electrolytes. In concentrated $ZnCl_2$, extended $[ZnCl_{4-m}^{2-m}]_n$ ionic networks ($n > 3$) have been observed, which compromise ionic conductivity and raise the desolvation penalty. Yang et al. introduced LiCl as a supporting salt to break Zn—Cl chains into shorter anionic clusters by increasing Li—Cl contacts, thereby creating a high entropy electrolyte while preserving conductivity.[33] However, because Zn—Cl bonding is stronger than Zn-H_2O coordination, such halogenated solvation shells can increase the desolvation barrier and risk halogen evolution reactions.[34] Although pure $Zn(OAc)_2$ has limited solubility (≈1.6 M), the acetate (OAc^-) anion, with flexible mono-/bidentate coordination and bidentate bridging coordination, enables, dynamic solvation and higher effective concentrations via hydrotropic solubilization.[35] Yet, similarly, high ionic strength in bisalt concentrated electrolyte reduces the Debye length, leaving strong ion pairing ($Zn^{2+}\cdots OAc^-$ and $K^+\cdots OAc^-$) and ordered aggregates unresolved (**Figure 1a**).[36]

Herein, we report a high-entropy flexible electrolyte (HEFE) that exploits the disparate, rapid water-exchange kinetics (Figure S1, Supporting Information) and asymmetric coordination environments of mixed Li^+, K^+, and Cs^+ cations. These monovalent cations were selected for three reasons (Table S1, Supporting Information): 1) they increase configurational entropy within localized ionic clusters and the hydrogen-bond network; 2) they contribute minimally to viscosity, preserving electrolyte fluidity; and 3) their differing charge densities promote a disordered ionic environment that disrupts ion pairing and hydrogen-bond networks, inhibits interfacial hydrogen-down water alignment, and suppresses cluster formation.[37,38] By tailoring hydration asymmetry among these cations, we engineer flexible solvated Zn complexes, predominantly $Zn(H_2O)_m^{2+}$($m \leq 6$), and induce disordered water configurations within the HEFE, yielding superior ionic conductivity and facilitating interfacial ion transport. Notably, a dynamic desolvation process of flexible Zn^{2+} characterized by a reduced desolvation barrier and accelerated kinetics is revealed, effectively suppressing HER and enabling exceptional long-term cycling stability. At the iodine cathode, HEFE drives a mechanistic shift from a liquid-to-solid pathway to a solid–solid conversion, inhibiting iodide shuttling and improving durability.

2. Results and Discussion

A multi-cation HEFE was formulated by mixing 4 M LiOAc, 4 M KOAc, 4 M CsOAc, and 4 M $Zn(OAc)_2$. This composition promotes a disordered solvation structure with a stoichiometrically unbalanced inner-shell hydration, effectively suppressing $Zn(OAc)_2{\cdot}2H_2O$(s) crystallization (Figure S1, Supporting Information). For comparison, a similar hydrotropic electrolyte (12 M KOAc/4 M $Zn(OAc)_2$: HTE) and a baseline 1 M $Zn(OAc)_2$ electrolyte were also prepared. Zn^{2+} solvation dynamics in HEFE, HTE, and baseline 1 M $Zn(OAc)_2$ were systematically interrogated via nuclear magnetic resonance (NMR) and Raman spectroscopies to elucidate structural and coordination disparities. As shown by the NMR spectra in Figure 1b, resonances at 1.8 ppm (H–C in acetate anions) and 4.7 ppm (H–O in H_2O) exhibit distinct chemical-shift changes across the electrolytes.[33,35] In HEFE, a more pronounced redshift of the water resonance and blueshift of the acetate resonance are observed relative to HTE and 1 M $Zn(OAc)_2$. These shifts are consistent with more effective shielding of water protons, indicative of reduced water activity, and with a transition of acetate coordination from bidentate to monodentate in HEFE.

Three O—H vibrational modes were quantified by Raman spectroscopy (Figure 1c,d): strong hydrogen bonds (tightly bound $H_2O\cdots H_2O$), weak hydrogen bonds (loosely bound $H_2O\cdots OAc^-$), and non-hydrogen-bonded water (free H_2O).[27,35] Relative to the 1 M $Zn(OAc)_2$ electrolyte, the fraction of strongly hydrogen-bonded water in HEFE was nearly halved, while the fraction of non-hydrogen-bonded water increased from 9% to 25%. In HTE, only a ~10% decrease in strong ($H_2O\cdots H_2O$) bonding was observed, accompanied by overall increases in the non-hydrogen-bonded and weakly hydrogen-bonded fractions. The substantial free-H_2O component in HTE and HEFE was attributed to the moderate effective concentration and the hydrophobic effect of the acetate groups.[26,30] Collectively, these results indicate a more disordered water structure in HEFE than in HTE; this interpretation is further supported by first-principles molecular dynamics (Figure S3, Supporting Information), in which a

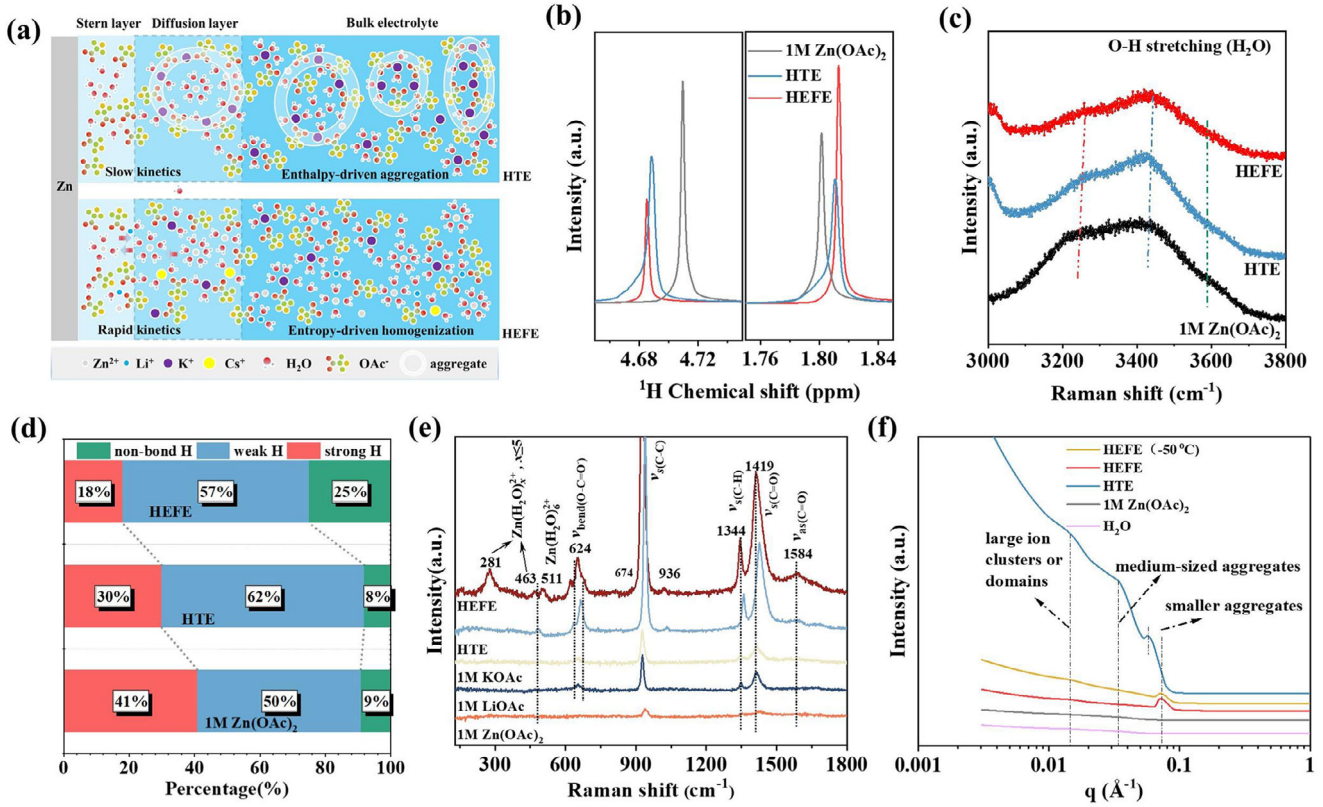

Figure 1. a) Entropy-guided design of a flexible electrolyte via unbalance of shell water with diverse flexible cations. b) ^{1}H NMR spectra of (right) OAc^- and (left) water in 1 M $Zn(OAc)_2$, HTE, and HEFE. c) Raman spectra of 1 M $Zn(OAc)_2$, HTE, and HEFE collected between 3000 and 3500 cm^{-1} as well as d) the percentage of fitted area for strong hydrogen-bond water, weak hydrogen-bond water, and non-hydrogen-bond water in the Raman spectra. e) Raman spectra of 1 M $Zn(OAc)_2$, 1 M LiOAc, 1 M KOAc, HTE, and HEFE collected between 150 and 1500 cm^{-1}. f) SAXS data for acetate-based concentrated electrolytes (i.e., HTE, HEFE, and HEFE at −50 °C), dilute 1 M $Zn(OAc)_2$, and pure water.

marked reduction in hydrogen bonding was observed. In addition to water structuring, the Zn^{2+}-H_2O interaction plays a critical role in electrochemical reversibility. To interrogate this interaction, low-frequency Raman spectra were collected (Figure 1e). In the 1 M $Zn(OAc)_2$ electrolyte, distinct vibrations associated with solvated Zn^{2+} were not observed, consistent with dominant bidentate acetate coordination. Signals from hydrated $M(H_2O)_n^+$ species with rapid inner-outer-sphere exchange, resulting in an asymmetric and flexible solvation structure, were likewise broadened and weak, rendering them difficult to detect. By contrast, while a single solvation structure of $[Zn(H_2O)_6]^{2+}$ appears at ≈511 cm^{-1} in the HTE, three distinct peaks at ≈281, 463, and 511 cm^{-1} are observed for the HEFE, corresponding to Zn—O vibrations in $[Zn(H_2O)_x]^{2+}$ ($x \leq 5$) respectively.[33] The broadness of $[Zn(H_2O)_x]^{2+}$ ($x \leq 5$) band at 281 cm^{-1} indicates a disordered solvation environment, consistent with outer-sphere ···OAc^- interactions arising from electrostatics and weak hydrogen bonding that modulate solvation flexibility.[37]

Analogous trends were reflected in acetate modes. The O—C=O bending vibrational (620–700 cm^{-1}) was split into two peaks in HTE relative to dilute OAc^- electrolytes.[39] This is attributed to the high ionic strength and derived ultrashort Debye length in the concentrated electrolyte, which brings about strong ion···OAc^- pairing and multiple coordination states (Table S2, Supporting Information). However, this enthalpy-driven hydrotropic solubilization also benefits aggregated clusters such as monodentate oligomeric chains like ···K^+-OAc^-- K^+-OAc^-··· or ··· K^+-OAc^--Zn^{2+}-OAc^-···, that localize structure and retard ion migration (Figure S4b, Supporting Information).[36,40] The resulting symmetry breaking around Zn^{2+} rendered certain Zn-centered modes weak or undetectable. In HEFE, the O—C=O bending band was split into three components, consistent with diverse OAc^- pairing states among four cations (Zn^{2+}, K^+, Li^+, Cs^+) and with rapid ligand exchange (~10^7–10^9 s^{-1}) between H_2O and OAc^-. The C=O asymmetric stretch at 1584 cm^{-1} was intensified, indicating enhanced polarizability changes and disorder due to OAc^- coordination to multiple cations. Owing to the compressed Debye length ($\kappa^{-1} \approx 1.6$ Å), partial and dynamic dehydration to $[Zn(H_2O)_x]^{2+}$···OAc^- and $[Zn(H_2O)_{x-1}]^{2+}$ ···OAc^- is facilitated, imparting solvation flexibility beneficial for interface reactions. Thus, stability is enhanced by the synergy of electrostatic interactions and weak hydrogen bonding with OAc^- (Figure S5, Supporting Information). Owing to its sensitivity to nanometer-scale electron-density variations, small-angle X-ray scattering (SAXS) was employed to probe aggregate and ordered structures in the acetate-based concentrated electrolytes (Figure 1f). Three main peaks are observed in the scattering vector range of q from 0.001 to 0.1 $Å^{-1}$, corresponding to a hierarchy of structural features: large ion clusters, medium-sized aggregates, and smaller aggregates. Across all electrolytes, the

features are best assigned to correlation peaks of polydisperse aggregates/ion clusters, as indicated by their non-harmonic peak ratios. Consistent with prior analysis, the total 16 M concentration in HTE promotes ion pairing and OAc^--bridged nanostructuring, yielding polydisperse, hierarchical clusters.[28] In contrast, the diffraction intensities at $q = 0.015$ and 0.034 $Å^{-1}$ decrease sharply, and the peak at $q \approx 0.057$ $Å^{-1}$ shifts to higher q, indicating fragmentation of larger clusters into smaller ones. This behavior is attributed to variations in metal–oxygen binding energies and coordination numbers among the mixed cations (Zn^{2+}, K^+, Li^+, Cs^+), which disrupt otherwise extended OAc^- chains into shorter, disordered pairs, thereby increasing configurational entropy and facilitating ionic conductivity (Table S3 and Figure S4d, Supporting Information). Even at −50 °C, no apparent aggregating is noted, proving the homogenous high-entropy electrolyte. To demonstrate our design principle for the high-entropy solution, the thermodynamic change accompanied by temperature and the solid-liquid transitions of three different electrolytes were explored by differential scanning calorimeter (DSC).As demonstrated in Figure S4e (Supporting Information), it is found that the electrolytes show various solid-liquid transitions, including glass-liquid transition, cold crystallization, melting, eutectic, and salt dissolving. In HTE, the glass transition at ca. −87 °C supports low-temperature performance, but the crystallization of $K_xZn_y(OAc)_{x+2y}{\cdot}nH_2O$ at −38 °C hampers low-temperature operation by reducing ionic conductivity. The endothermic peak at 22 °C indicates dydrate dissolution to form aggregates and confirms the non-eutectic nature of HTE. In contrast, no endo- or exothermic peaks but a glass transition step at −91 °C reflects the liquid-like disordered structures in HEFE, indicating kinetic and thermodynamic stabilization against ordered phase and confirming configurational diversity of Zn-ion solvation shells and high entropy ($\Delta G_{mix} = \Delta H_{mix} - T\,\Delta S_{mix}$).[7]Concurrently, the disordered water network breaks continuous strong H-bond chains required for efficient Grotthuss proton hopping and mitigates H-down water alignment near cathodes under interfacial electric fields.[12]

The electrochemical performance of the three electrolytes was systematically evaluated using Zn//Cu half-cells and Zn//Zn asymmetric cells. Linear sweep voltammetry (LSV) revealed stark differences in stability (**Figure 2a**). The 1 M $Zn(OAc)_2$ electrolyte exhibited the highest Zn deposition current but suffered catastrophic failure due to severe HER and dendritic growth, highlighting its thermodynamic instability. In contrast, the HTE extended the operation voltage window to −1.5 V but displayed inferior Zn deposition kinetics, a consequence of suppressed water reactivity at the cost of diffusion-limited ion transport typical of concentrated electrolytes. This sluggish ion transport fostered an electrode-electrolyte interface (EEI) with ordered water, further exacerbating polarization and dendrite formation. Notably, the HEFE synergistically combined a wide 3 V stability window with elevated reduction currents, indicative of rapid, unimpeded Zn^{2+} migration and a stabilized EEI. Tafel analysis further corroborated the superior corrosion resistance of HEFE, showing a higher corrosion potential and lower corrosion current compared to its counterparts (Figure 2b). It is compared in the Cyclic voltammetry (CV) recorded at 3 mVs^{-1} that HEFE is characterized by minimal voltage hysteresis of 0.39 V among three electrolytes (Figure 2c), and CV collected from 5 to 20 mVs^{-1} further revealed the pseudocapacitive redox behavior of HEFE, indicating highly reversible Zn plating/stripping dominated by high surface-controlled processes with ultrafast interfacial kinetics (Figure 2d; Figure S6, Supporting Information). These features were quantitatively supported by the reduced interfacial resistance observed in electrochemical impedance spectroscopy (EIS) (Figure 2e). The practical viability of HEFE was validated through long-term cycling tests: Zn//HEFE//Cu cells achieved 2100 cycles at 2 mA cm^{-2} with a Coulombic efficiency of 99.4% in the first 800 cycles, markedly outperforming the HTE and 1 M $Zn(OAc)_2$ electrolytes, which failed prematurely due to separator perforation (Figure 2f). Even under stringent conditions with 50% Zn utilization, Zn//HEFE//Zn symmetric cells sustained 450 h of stable operation with minimal voltage hysteresis (≈100 mV) across current densities ranging from 0.5 to 5 mA cm^{-2} (Figure 2g). This exceptional performance is attributed to the entropy-engineered solvation structure in HEFE, which suppresses HER, facilitates Zn^{2+} desolvation through dynamic monodentate acetate coordination, and reduces interfacial resistance via enhanced high-entropy ion transport, collectively advancing the development of Zn-based energy storage systems.

A detailed investigation into the mechanism of Zn plating and stripping at the anode was conducted using in situ surface enhanced Raman spectra (SERS), in situ x-ray diffraction (XRD), operando gas chromatography (GC), and density-functional theoretical (DFT) calculations. SERS analysis (**Figure 3a,b**) identified three distinct O—H stretching bands in the interfacial region: i) 4-coordinated hydrogen-bonded water (4-HB·H_2O) at low wavenumbers, ii) 2-coordinated hydrogen-bonded water (2-HB·H_2O) as the dominant mid-wavenumber component, and iii) Zn^{2+}-hydrated water ($Zn^{2+}{\cdot}H_2O$) with weak hydrogen bonds at high wavenumbers.[41] Under negative bias, conventional electrolytes (HTE) exhibited a pronounced $Zn^{2+}{\cdot}H_2O$ band, indicative of a H-down interfacial configuration that accelerates hydrogen evolution (Figure 3a). In contrast, the HEFE showed no such shift; instead, the 4-HB·H_2O band intensified upon application of a −0.3 V bias (Figure 3b), suggesting cation-driven restructuring of solvation shells to suppress free water activity. Further Raman analysis in the 100–600 cm^{-1} range (Figure 3c) was conducted to track solvation dynamics under applied bias. Vibrational peaks corresponding to the solvated structures $[Zn(H_2O)_6]^{2+}$ (511 cm^{-1}), $[Zn(H_2O)_x]^{2+}$ ($x \leq 5$) (463, 281 cm^{-1}) all exhibited a progressive decline in intensity, indicating the desolvation and subsequent reduction of hydrated Zn^{2+} ions.[33,42] Notably, the ratio of $[Zn(H_2O)_x]^{2+}$ ($x \leq 5$) to $[Zn(H_2O)_6]^{2+}$ increased sharply at a bias of −0.3 V, suggesting the dynamic reconstruction of the solvation shell. This behavior indicates that a portion of $[Zn(H_2O)_6]^{2+}$ ions are transformed into $[Zn(H_2O)_x]^{2+}$ ($x \leq 5$) species with favorable thermodynamics and hydrogen-bond assistance prior to the final reduction step (Figure 3d).[43,44] DFT calculations (Figure 3e) corroborated this observation, revealing that $[Zn(H_2O)_x]^{2+}$($x \leq 5$) exhibits a lower desolvation energy barrier compared to $[Zn(H_2O)_6]^{2+}$, thus favoring this dynamic desolvation pathway and blocking one of the traditional HER pathways: electric-driven H-down orientation in shell water. Additionally, XRD analysis (Figure 3f) showed suppressed growth of the Zn (101) facet in HEFE, promoting dense deposition morphologies over dendritic structures, a phenomenon similarly observed for Mn^{2+} deposition (Figures S7 and S8, Supporting Information). Complementarily, operando GC confirmed the

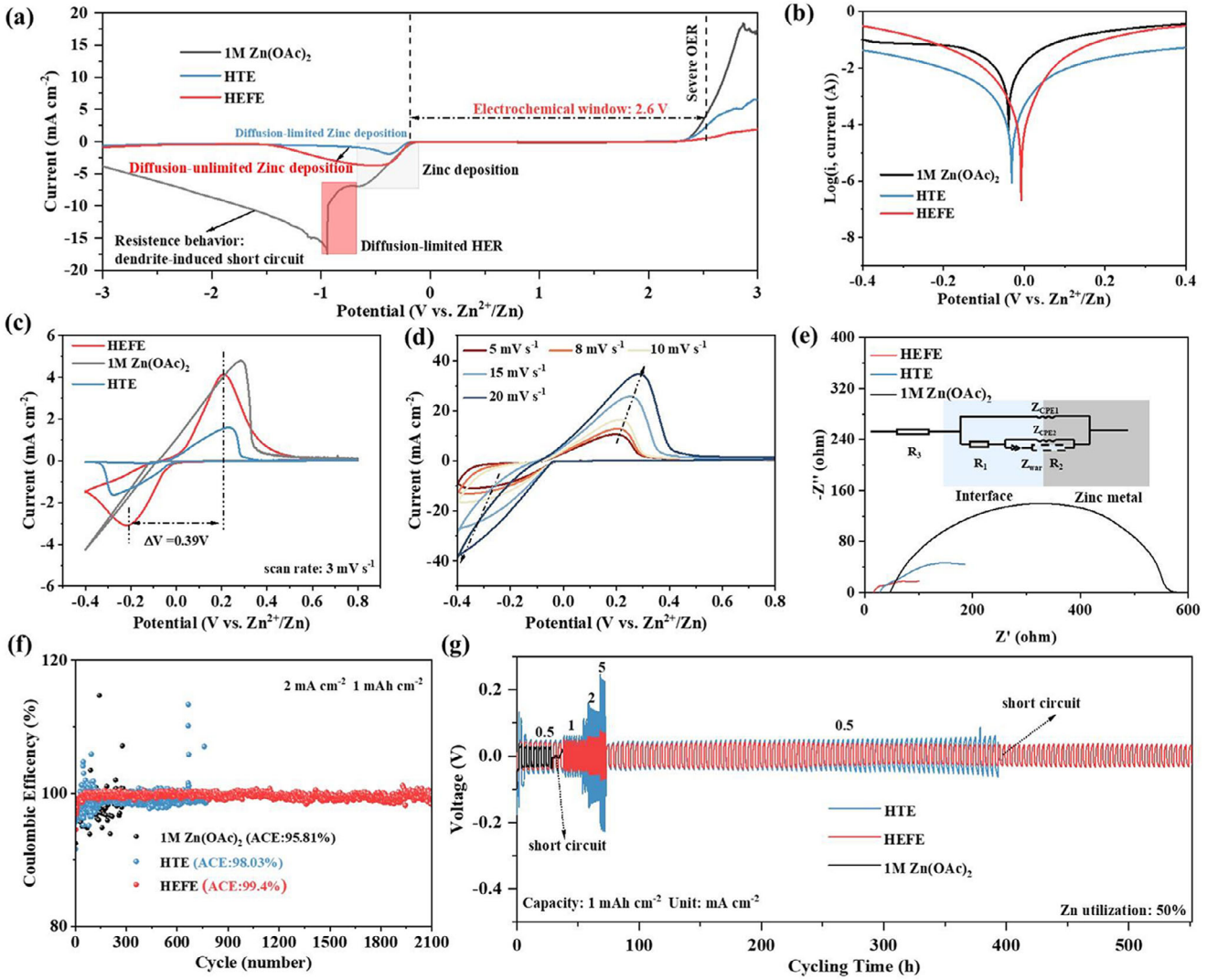

Figure 2. a) LSV curve of Zn//Cu half cells, b) Tafel plot, and c) CV profiles in 1 M $Zn(OAc)_2$, HTE, and HEFE electrolytes. d) CV curves of Zn//Cu half cell in HEFE collected at high sweeping rates. e) EIS spectra of Zn//Zn symmetric cell in three different electrolytes. f) Long-term cycling performance comparison of Zn//Cu half cell in the 1 M $Zn(OAc)_2$, HTE, and HEFE three electrolytes with average coulombic efficiency of first 200, 600, and 800 cycles respectively. g) Rate and cycling performance of Zn//Zn symmetric cell in three different electrolytes with a capacity of 1 mAh cm^{-2}.

suppression of HER in HEFE, showing negligible hydrogen evolution compared to the 1 M $Zn(OAc)_2$ and HTE electrolytes, aligning with the stable pH observed during cycling (Figure 3g–j; Figure S9, Supporting Information).

Scanning electron microscopy (SEM) analyses (**Figure** 4a–d) provided critical insights into the morphological evolution of Zn deposition in different electrolytes. In the HEFE, the Zn deposits exhibited a remarkably uniform and compact layer structure, demonstrating the effectiveness of the engineered solvation environment in promoting homogeneous nucleation and growth. In stark contrast, the HTE led to uneven surface bumps, a consequence of severe ion depletion near the electrode surface. The growth of bump-like dendrites is attributed to interfacial, dynamically OAc^--bridged small nanoclusters bearing hydrophobic methyl groups. These clusters create a micelle-like environment that favors isotropic growth and promotes a networked deposition pattern.[8,11,30] Meanwhile, the conventional 1 M $Zn(OAc)_2$ electrolyte resulted in pronounced dendritic structures, which were primarily driven by HER-induced local pH fluctuations and uncontrolled Zn^{2+} reduction (Figure S10, Supporting Information). To further elucidate the underlying mechanisms, COMSOL Multiphysics simulations (Figure 4e,f) were employed to model ion transport and concentration gradients during plating. The simulations confirmed that the high-entropy design of HEFE significantly enhanced Zn^{2+} mobility by mitigating concentration polarization, a key factor in achieving dendrite-free deposition. This entropy-enhanced ion transport ensured a steady supply of Zn^{2+} to the electrode interface, preventing localized depletion and promoting smooth Zn growth. The superior electrochemical performance of HEFE was further validated by long-term cycling tests in symmetric Zn//HEFE//Zn cells (Figure 4g,h; Figure S11, Supporting Information). The cells

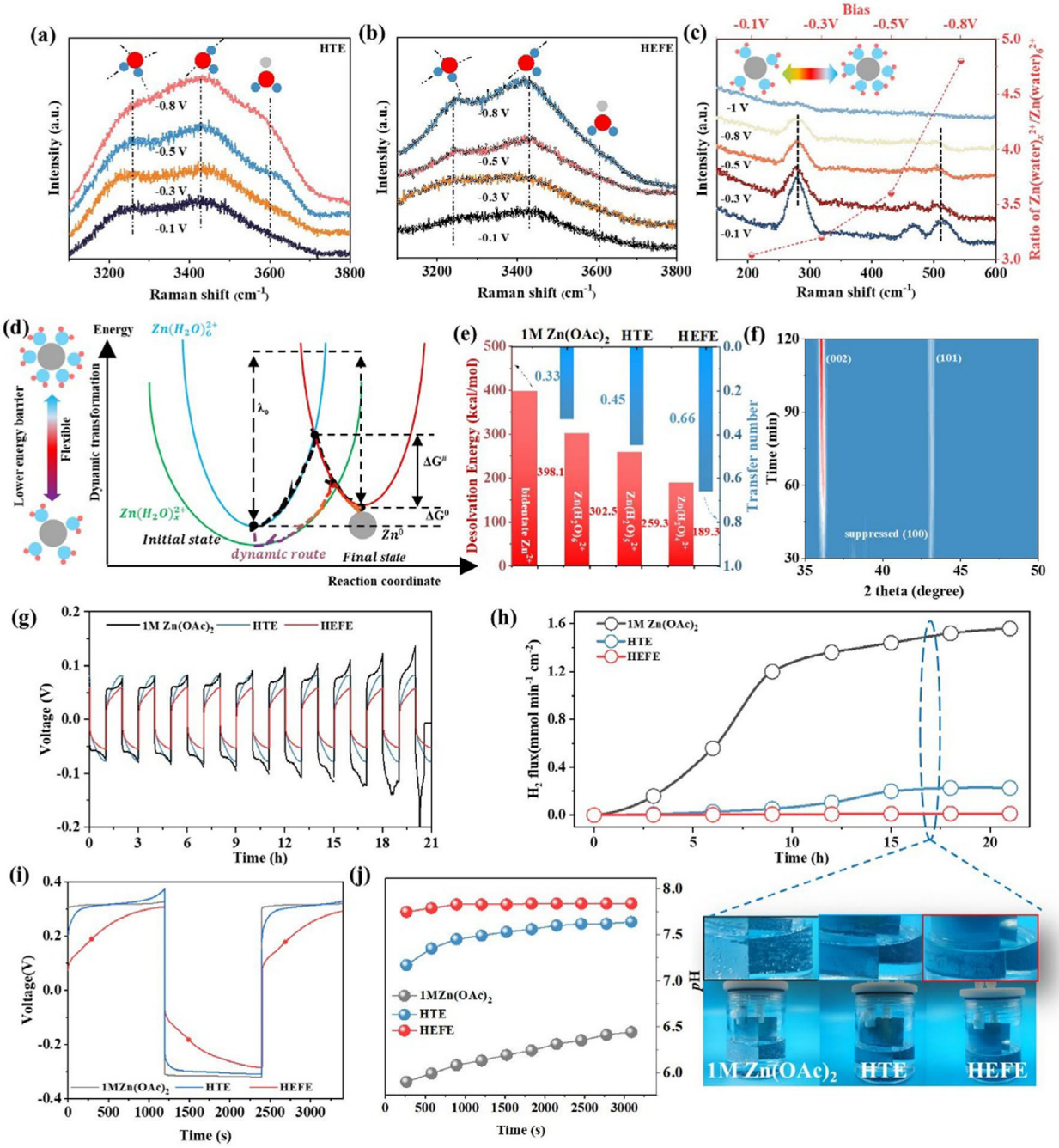

Figure 3. Surface enhanced Raman spectra in the range focusing on interfacial water behavior in a) HTE and b) HEFE electrolytes. c) Surface enhanced Raman spectra in the range focusing on interfacial solvated $Zn(H_2O)_6^{2+}$ and $Zn(H_2O)_x^{2+}$ ($x \leq 5$) behavior. d) Energy scheme of dynamic and flexible desolvation process based on Marcus theory. e) Desolvation energy of different solvated structures and measured transfer number of Zn ions in different electrolytes. f) In situ XRD pattern of deposited Zn at 1 mA cm^{-2}. g) electrochemical cycling of Zn symmetric cell at 2 mA cm^{-2} and g) in situ detection of hydrogen generation in the Zn symmetric cell. Inset: images of Zn symmetric cell: Left in 1 M $Zn(OAc)_2$, middle in HTE, and right in HEFE. i,j) In situ pH evolution during Zn deposition process at 10 mA cm^{-2}.

demonstrated exceptional stability over 145 days of continuous operation at 1 mA cm^{-2}/3 mAh cm^{-2}, far surpassing conventional electrolytes. This unprecedented durability stems from the synergistic effects of the flexible solvation structure of HEFE, which simultaneously optimizes Zn^{2+} migration and desolvation kinetics, suppresses HER, and regulates Zn deposition morphology. Sand's time (T_{sand}) was used to assess plating stability and reversibility. A shorter T_{sand} in HTE suggests reduced charge transfer, attributable to aggregate trapping and interfacial ion depletion, which in turn promotes Zn dendrite formation and HER (Figure S12, Supporting Information).[5] This interpretation is consistent with the asymmetric voltage profiles observed during

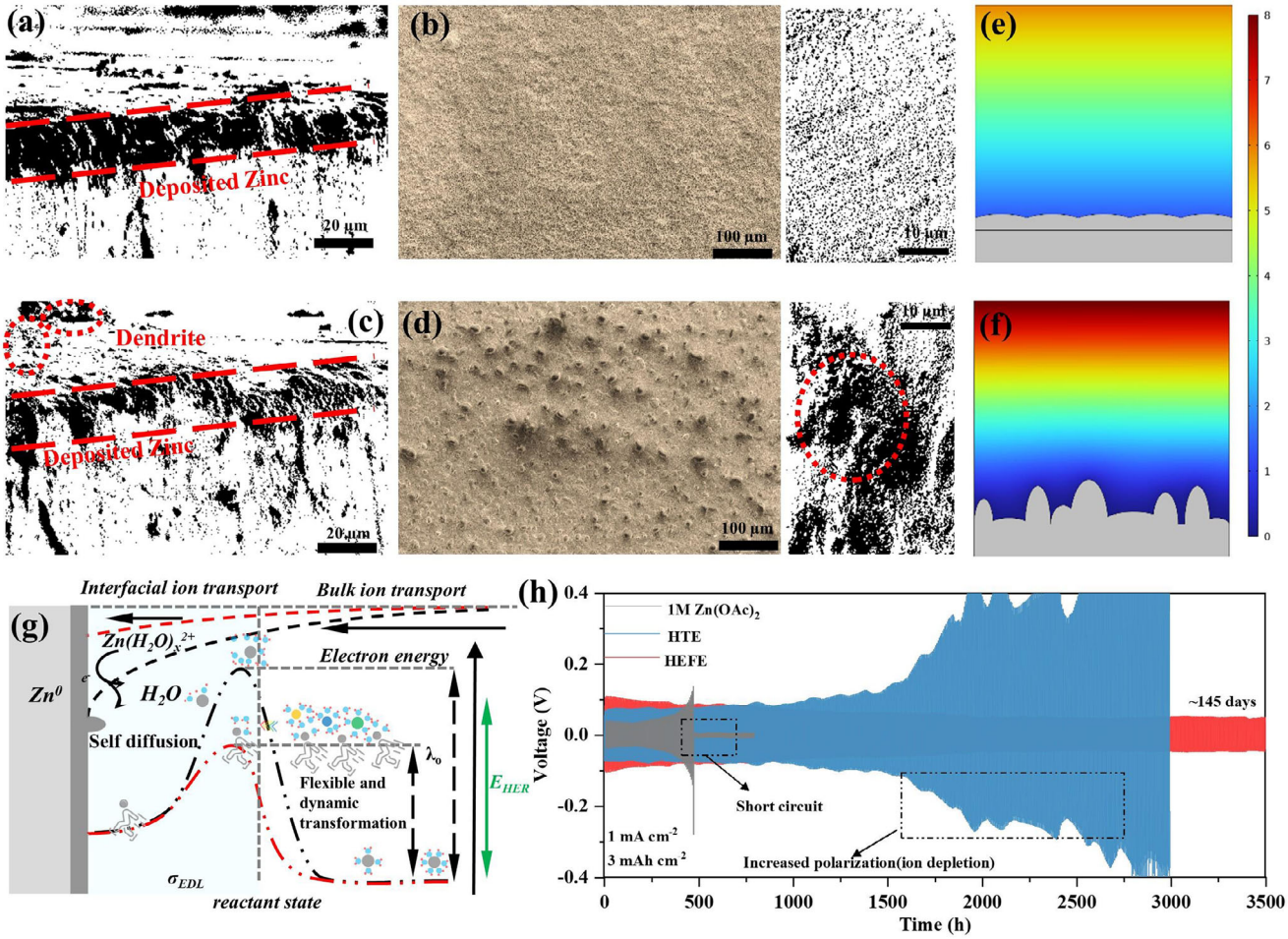

Figure 4. SEM images of deposited Zn in a,b) HTE electrolyte and c,d) HEFE electrolyte at 5 mA cm^{-2}/5 mAh cm^{-2}. COMSOL simulation analysis of the Zn dendrite growth and concentration distribution in e) HEFE and f) HTE. g) Interfacial electrochemistry diagram of comparing ion desolvation process in HTE and HEFE electrolyte. h) Long-term cycling performance comparison of Zn//Zn symmetric cell using the 1 M $Zn(OAc)_2$, HTE, and HEFE electrolytes.

cycling. Collectively, these results underscore the superior electrochemical performance of HEFE relative to prior reports (Table S4, Supporting Information) and underscore the critical role of electrolyte engineering in enabling stable Zn-metal anodes for next-generation energy-storage technologies.

Electrolytes were evaluated in full-cell configuration using a carbon-supported iodine cathode, addressing the persistent issue of iodide shuttling during cycling. This phenomenon, driven by the dissolution of active iodine species (e.g., I^-/I_2 redox couples) into the electrolyte, leads to irreversible capacity loss in conventional systems. To address this issue, we engineered a solid-to-solid reaction (SSR) mechanism within the HEFE electrolyte, leveraging the low solubility of cesium iodide (CsI) and the structural advantages of high-entropy concentrated electrolytes. This strategy effectively replaces the conventional liquid-to-solid reaction pathway, mitigating iodine dissolution and enhancing cycling stability. When tested under two-electron transfer conditions, the iodine@C cathode delivered 420 mAh g^{-1} in HEFE, exceeding the capacity obtained in HTE (**Figure 5a**). Well-defined redox peaks at 1.7 and 1.2 V indicate a highly reversible SSR process. By contrast, HTE, prone to iodine dissolution, exhibited reduced efficiency. In situ Raman spectroscopy (Figure 5b; Figure S13, Supporting Information) revealed critical interfacial species in HEFE, a peak at 117 cm^{-1} (CsI) and two small peaks at 240 and 307 cm^{-1} (iodine-Zn species).[45] During charging to ca. 1.3 V, the gradual attenuation of these peaks indicated the conversion of CsI into I_2, confirming the SSR mechanism. In situ XRD (Figure S14, Supporting Information) further validated this reversibility, with distinct peaks at 27° and 48° corresponding to crystalline CsI, a phase with minimal aqueous solubility.[46] Control experiments in a hybrid Zn^{2+}/Cs^+ electrolyte confirmed the dominance of the CsI-mediated redox reaction, evidenced by shifted redox peaks from 1.2 V/1.25 V (I^-/I_2) to 1.32 V/1.42 V (CsI/I_2), underscoring the role of solubility in stabilizing iodine (Figure S15, Supporting Information). The enhanced kinetics of HEFE were further quantified using Dunn's method, revealing a capacitive contribution of 78.1% (Figure 5c,d), approximately 10% higher than that of HTE, attributed to high-entropy-enhanced ion mobility and structural flexibility. This kinetic advantage translated into exceptional cycling stability: the HEFE-based cathode

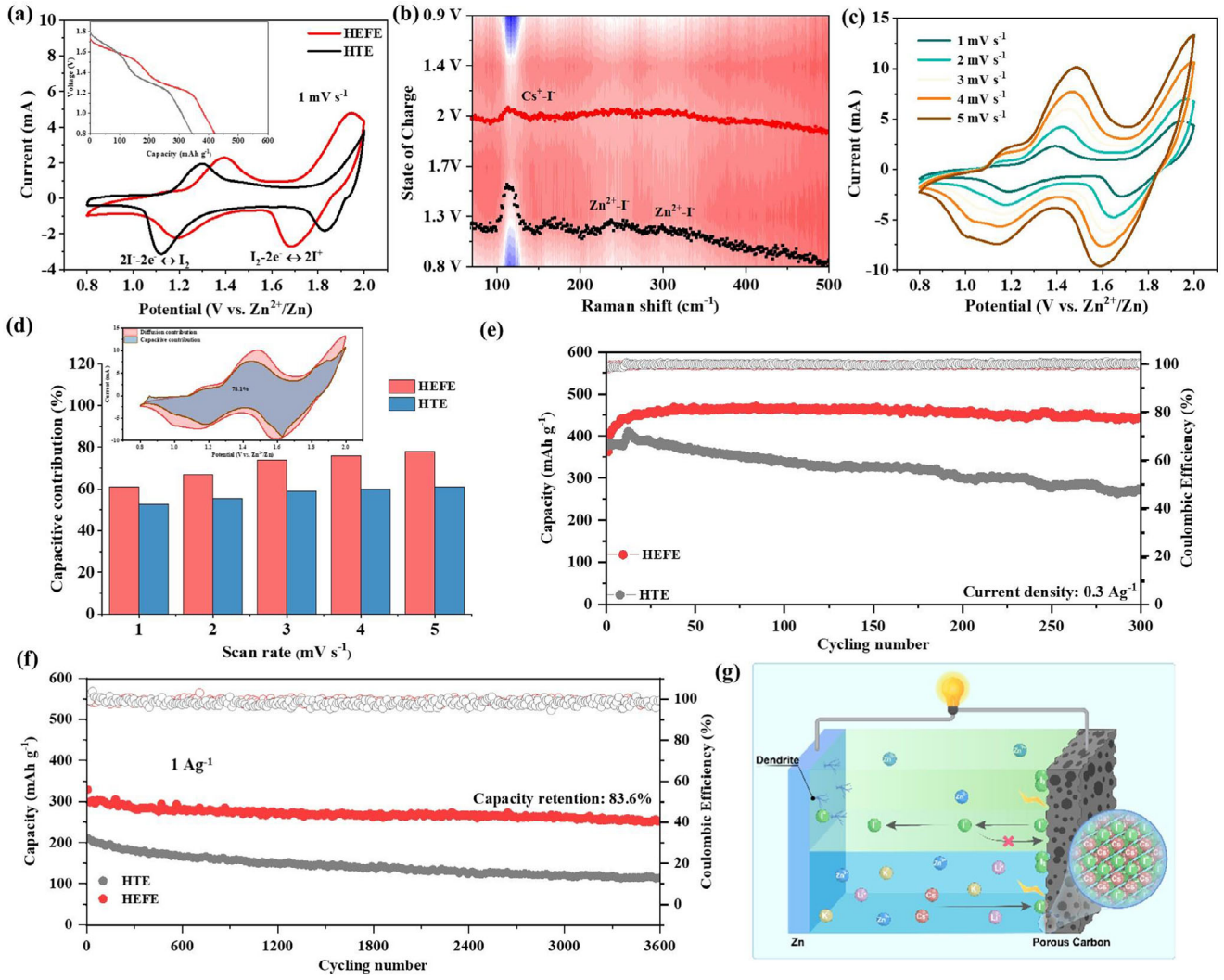

Figure 5. a) Comparison of the corresponding CV profiles of I_2@C in HEFE, HTE. Inset: Corresponding galvanostatic discharge curve. b) In situ Raman spectra of I_2@C cathode collected during charge/discharge process in HEFE electrolyte. c) CV profiles recorded from 1 to 5 mV s^{-1} in HEFE electrolyte and d) capacitive contribution to the energy storage extracted via Dunn Method from CV profile. Cycling test of iodine@C in HTE and HEFE at current density e) 0.3 Ag^{-1} and f) 1A g^{-1}. g) Illustration of shuttling-inhibiting effect of cesium cations in an aqueous Zn-iodine battery.

retained 443 mAh g^{-1} after 300 cycles at 0.3 A g^{-1}, and 252 mAh g^{-1} after 3600 cycles at 1 A g^{-1} (Figure 5e–g), outperforming previously reported iodine cathodes (Figure S16 and Table S5, Supporting Information). Furthermore, the universality of HEFE was demonstrated in aqueous Zn/$LiMnO_4$ and Zn/$LiFePO_4$ systems (Figures S17 and S18, Supporting Information), underscoring its versatility for advanced aqueous energy storage applications.

3. Conclusion

In summary, we developed a HEFE by harnessing the rapid shell-water exchange dynamics of flexible cations, specifically Li^+, K^+, and Cs^+. By strategically introducing an imbalance in coordinated water molecules across different cations, we engineered a diverse and flexible solvation structure, comprising $Zn(H_2O)_6^{2+}$ and $Zn(H_2O)_x^{2+}$ ($x \leq 5$) species, and induced a disordered water configuration within the HEFE matrix. This unique solvation landscape imparts exceptional ionic conductivity, a key parameter for enhancing interfacial ion transport. Under negative electrochemical bias, SERS revealed a dynamic desolvation process wherein $Zn(H_2O)_6^{2+}$ species progressively transform into $Zn(H_2O)_x^{2+}$ ($x \leq 5$) prior to electrochemical reduction. This dynamic pathway, characterized by a reduced thermodynamic barrier and accelerated kinetics, effectively suppresses hydrogen evolution. As a result, the HEFE delivers outstanding long-term cycling stability, sustaining over 3500 h at 1 mA cm^{-2} with a capacity of 3 mAh cm^{-2}. Furthermore, in situ Raman spectroscopy and XRD analyses uncovered a fundamental shift in the redox mechanism of iodine-based cathodes within the HEFE environment. The conventional liquid-to-solid transformation ($2I^- - 2e^- \rightarrow I_2$) is supplanted by an SSR redox pathway ($2CsI(s) - 2e^- \rightarrow 2Cs^+ + I_2(s)$), enabled by modulated iodide solubility and the physicochemical benefits of concentrated electrolytes, effectively inhibiting iodide shuttling. Consequently, Zn//HEFE//Iodine@C cells

exhibit exceptional electrochemical durability, retaining performance over 3600 cycles at 1 A g^{-1}. This work thus charts a promising pathway toward next-generation, high-performance electrochemical energy storage technologies.

4. Experimental Section

Preparation of High-Entropy Flexible Electrolyte: All chemicals were used in their as-received state. The high-entropy flexible electrolyte(4 M LiOAc, 4 M KOAc, 4 M CsOAc, and 4 M $Zn(OAc)_2$), which was fabricated by hydrotropic solubilization agents, was stoichiometrically formulated by combining $Zn(Ac)_2$ (having a purity greater than 99%) and hydrotropic flexible agents (LiOAc/KOAc/CsOAc, all with a purity above 99%) with deionized water at 25 degrees Celsius. All chemicals were sourced from Aladdin, apart from LiOAc (acquired from Sigma–Aldrich) and Cesium acetate (bought from Sigma–Aldrich). The conventional hydrotropic electrolyte was prepared by merely dissolving potassium acetate and Zn acetate in purified water.

Preparation of Iodine@C Cathode: The cathodes were prepared using the solution-adsorption method. Briefly, 10 mg of I_2 was combined with 10 mg of porous active carbon, after which 20 mL of deionized water was added. The iodine content in the I_2@C composite was ≈15–20 wt.%. This was calculated by subtracting the mass of carbon from the total mass of the final weighed composite. Next, I_2@C, NMP, and Super P were mixed in ethanol at a mass ratio of 7:2:1. Subsequently, the resulting slurry was cast onto a carbon cloth with a diameter of 1cm. After that, it was dried in air at 60 °C for 6 h. The electrodes were then cut into disks. The average areal loading of the I_2@C composite in the electrode was ≈2–3 mg cm^{-2}.

Supporting Information

Supporting Information is available from the Wiley Online Library or from the author.

Acknowledgements

R.P. and Y.X. contributed equally to this work. This work was supported by the National Natural Science Foundation of China (12174050, 52473270, T2321002 and T2422028), the National Key R&D Program of China (2022YFA1203304), the Natural Science Foundation of Jiangsu Province (BK20231411 and BK20222007), the Suzhou Institute of Nano-Tech and Nano-Bionics, Chinese Academy of Sciences (Start-up grant E1552102), the Postgraduate Research & Practice Innovation Program of Jiangsu Province (KYCX24_0500) and the Fundamental Research Funds for the Central Universities. The authors are grateful for the technical support of SAXS from Qing Zhang for Nano-X Suzhou Institute of Nano-Tech and Nano-Bionics, Chinese Academy of Sciences.

Conflict of Interest

The authors declare no conflict of interest.

Data Availability Statement

The data that support the findings of this study are available from the corresponding author upon reasonable request.

Keywords

aqueous electrolyte, dynamic desolvation, high-entropy electrolyte, iodide shuttle, zinc-iodine battery

Received: July 2, 2025
Revised: September 3, 2025
Published online: September 19, 2025

[1] C. Lu, H. Jiang, X. Cheng, J. He, Y. Long, Y. Chang, X. Gong, K. Zhang, J. Li, Z. Zhu, J. Wu, J. Wang, Y. Zheng, X. Shi, L. Ye, M. Liao, X. Sun, B. Wang, P. Chen, Y. Wang, H. Peng, *Nature* **2024**, *629*, 86.
[2] H. Jin, S. Xin, C.-H. Chuang, W. Li, H. Wang, J. Zhu, H. Xie, T. Zhang, Y. Wan, Z. Qi, W. Yan, Y.-R. Lu, T.-S. Chan, W.-W. Wu, J.-G. Goodenough, H. Ji, X. Duan, *Science* **2020**, *370*, 192.
[3] D. Lu, R. Li, M. M. Rahman, P. Yu, L. Lv, S. Yang, Y. Huang, C. Sun, S. Zhang, H. Zhang, J. Zhang, X. Xiao, T. Deng, L. Fan, L. Chen, J. Wang, E. Hu, C. Wang, X. Fan, *Nature* **2024**, *627*, 101.
[4] J. Shi, Y. Zhou, M. Chen, F. Zhang, X. Liu, W. Wang, L. Sun, Y. Cao, Z. Liu, K. Xu, C. Wang, *Nat. Mater.* **2024**, *23*, 1686.
[5] D. Lin, Y. Liu, Y. Cui, *Nat. Nanotech.* **2017**,*12*, 194.
[6] Y. Zhang, L. Yu, X.-D. Zhang, Y.-H. Wang, C. Yang, X. Liu, W.-P. Wang, Y. Zhang, X.-T. Li, G. Li, S. Xin, Y.-G. Guo, C. Bai, *Sci. Adv.* **2023**, *9*, ade5802.
[7] L. Jiang, S. Han, Y.-C. Hu, Y. Yang, Y. Lu, Y.-C. Lu, J. Zhao, L. Chen, Y.-S. Hu, *Nat. Energy* **2024**, *9*, 839.
[8] F. Wang, H. Li, X. Chen, Y. Xu, Z. Zhou, C. Wang, *Nat. Mater.* **2018**, *17*, 543.
[9] R. Pan, F. Cui, A. Zheng, G. Zhang, Z. Jiang, Y. Xiong, L. Wei, Q. Zhang, L. Sun, K. Yin, *Adv. Funct. Mater.* **2023**,*33*, 2300619.
[10] Q. Yang, P. Chen, X. Liu, H. Peng, C. Wang, *Adv. Mater.* **2020**, *32*, 2001854.
[11] Y. Li, X. Zheng, E. Z. Carlson, X. Xiao, X. Chi, Y. Cui, L. C. Greenburg, G. Zhang, E. Zhang, C. Liu, Y. Yang, M. S. Kim, G. Feng, P. Zhang, H. Su, X. Guan, J. Zhou, Y. Wu, Z. Xue, W. Li, M. Bajdich, Y. Cui, *Nat. Energy* **2024**, *9*, 1350.
[12] C. T. Wolke, J. A. Fournier, L. C. Dzugan, M. R. Fagiani, T. T. Odbadrakh, H. Knorke, K. D. Jordan, A. B. McCoy, K. R. Asmis, M. A. Johnson, *Science* **2016**, *354*, 1131.
[13] F. Wan, Z. Yang, X. Li, L. Zhao, M. Chen, Y. Sun, J. Zheng, *Nat. Commun.* **2018**, *9*, 1656.
[14] S. Wang, H. Zhou, X. Liu, Y. Zhang, J. Li, P. Zhao, M. Sun, Q. Luo, *Nat. Commun.* **2025**, *16*, 1800.
[15] L. Lin, Y. Huang, B. Zhao, C. Xu, D. Guan, F. Li, H. Zhang, X. Chen, S. Yang, *Angew. Chem., Int. Ed.* **2025**, *64*, 202425008.
[16] F. Bu, C. Zhao, M. Wang, Q. Liu, Y. Chen, H. Li, X. Zhou, L. Sun, *Angew. Chem., Int. Ed.* **2024**, *63*, 202318496.
[17] M. Qiu, Y. Wang, J. Liu, X. Chen, H. Zhao, L. Zhang, F. Gao, *Nat. Commun.* **2024**, *15*, 10420.
[18] M. Qiu, L. Sun, H. Zhao, X. Wang, P. Liu, J. Zhang, C. Chen, S. Li, *Adv. Mater.* **2025**, *37*, 2418947.
[19] D. Wang, J. Li, S. Zhao, L. Xu, M. Liu, Y. Huang, X. Chen, *Angew. Chem., Int. Ed.* **2025**, *64*, 202414117.
[20] J. Zhu, Y. Li, X. Zhang, H. Chen, Q. Sun, L. Wang, *Adv. Mater.* **2025**, *36*, 2304426.
[21] L. Cao, D. Li, T. Pollard, O. Borodin, J. Hu, T. Deng, C. Du, L. Chen, L. Ma, Q. Li, S. Hou, M. Disko, K. Gong, M. J. Heenan, J. T. Fourkas, K. Xu, C. Wang, *Nat. Nanotechnol.* **2021**, *16*, 902.
[22] Y. H. Wang, J. Y. Zheng, L. Chen, X. Liu, M. Sun, D. Li, S. Qin, H. Wang, *Nature* **2021**, *600*, 81.
[23] J. Wei, X. Zhou, Y. Li, H. Zhang, J. Sun, L. Wang, M. Yu, *Chem. Soc. Rev.* **2024**, *53*, 10335.
[24] D. L. Han, C. J. Cui, K. Y. Zhang, Z. X. Wang, J. C. Gao, Y. Guo, Z. C. Zhang, S. C. Wu, L. C. Yin, Z. Weng, *Nat. Sustain.* **2022**, *5*, 205.
[25] W. Yang, Z. Hu, X. Li, J. Chen, L. Guo, M. Zhang, *Joule* **2020**, *4*, 1557.
[26] D. Dong, C.-X. Zhao, X. Zhang, C. Wang, *Adv. Mater.* **2025**, *37*, 2418700.

[27] S. M. Hao, X. Li, Z. Zheng, J. Wu, H. Wang, *Nat. Sustain.* **2024**, *7*, 661.
[28] K. Qian, R. E. Winans, T. Li, *Adv. Energy Mater.* **2021**, *11*, 2002821.
[29] P. Ruan, J. Zhao, Y. Chen, Q. Liu, R. Wang, *Angew. Chem., Int. Ed.* **2022**, *61*, 202200598.
[30] L. Suo, O. Borodin, T. Gao, M. Olguin, J. Ho, X. Fan, C. Luo, C. Wang, K. Xu, *Science* **2015**, *350*, 938.
[31] H. Jiang, L. Tang, Y. Fu, S. Wang, S. Sandström, A. Scida, G. Li, D. Hoang, J. Hong, N.-C. Chiu, K. Stylianou, W. Stickle, D. Wang, J. Li, P. Greaney, C. Fang, X. Ji, *Nat. Sustain.* **2023**, *6*, 806.
[32] S. C. Kim, J. Wang, R. Xu, P. Zhang, Y. Chen, Z. Huang, Y. Yang, Z. Yu, S. T. Oyakhire, W. Zhang, L. C. Greenburg, M. S. Kim, D. T. Boyle, P. Sayavong, Y. Ye, J. Qin, Z. Bao, Y. Cui, *Nat. Energy* **2023**, *8*, 814.
[33] C. Yang, J. Xia, C. Cui, T. P. Pollard, J. Vatamanu, A. Faraone, J. A. Dura, M. Tyagi, A. Kattan, E. Thimsen, J. Xu, W. Song, E. Hu, X. Ji, S. Hou, X. Zhang, M. S. Ding, S. Hwang, D. Su, Y. Ren, X. Yang, H. Wang, O. Borodin, C. Wang, *Nat. Sustain.* **2023**, *6*, 325.
[34] L. Chang, H. Cheng, J. Li, L. Zhang, B. Zhang, L. Zheng, Q. Sun, J. Li, X. Lu, K. Zhao, *Nat. Commun.* **2025**, *16*, 6134.
[35] D. Dong, T. Wang, Y. Sun, J. Fan, Y.-C. Lu, *Nat. Sustain.* **2023**, *6*, 1474.
[36] J. Zheng, G. Tan, P. Shan, T. Liu, J. Hu, Y. Feng, L. Yang, M. Zhang, Z. Chen, Y. Lin, J. Lu, J. C. Neuefeind, Y. Ren, K. Amine, L.-W. Wang, K. Xu, F. Pan, *Chem* **2018**, *4*, 2872.
[37] Y. Zhu, S. Thomas, T. Wang, X. Guo, Y. Wang, C. Liu, S. M. Sarathy, X. Zhang, O. M. Bakr, O. F. Mohammed, H. N. Alshareef, *Sci. Adv.* **2025**, *11*, adx8413.
[38] M. Qiu, D. Wang, Y. Sun, H. Zhao, C. Chen, S. Li, P. Zhang, L. Fan, J. Zhang, *Angew. Chem., Int. Ed.* **2024**, *63*, 202407012.
[39] Z. Nickolov, G. Georgiev, D. Stoilova, I. Ivanov, *J. Mol. Struct.* **1995**, *354*, 119.
[40] M. Li, X. Wang, J. Meng, C. Zuo, B. Wu, C. Li, W. Sun, L. Mai, *Adv. Mater.* **2024**, *36*, 2308628.
[41] C. Y. Li, N. Wang, P. Zhang, X. Sun, L. Zhao, Y. Huang, J. Gao, H. Peng, *Nat. Mater.* **2019**, *18*, 697.
[42] Q. Zhang, Y. Ma, Y. Lu, L. Li, F. Wan, K. Zhang, J. Chen, *Nat. Commun.* **2020**, *11*, 4463.
[43] M. Yang, J. Zhu, S. Bi, R. Wang, Z. Niu, *Adv. Mater.* **2022**, *34*, 2201744.
[44] R. Wang, M. Yao, M. Yang, J. Zhu, J. Chen, Z. Niu, *Proc. Natl. Acad. Sci. U. S. A.* **2023**, *120*, 2221980120.
[45] M. M. Metallinou, S. A. Johnson, R. Peters, J. K. Thompson, *Inorg. Chem.* **1991**, *30*, 4260.
[46] J. Deng, L. Li, H. Zhang, X. Wang, Y. Tian, *J. Sol. Gel Sci. Technol.* **2016**, *78*, 482.